



Supporting Online Material for

**The Impact of Comet Shoemaker-Levy 9
Sends Ripples Through the Rings of Jupiter**

Mark R. Showalter,* Matthew M. Hedman, Joseph A. Burns

*To whom correspondence should be addressed. E-mail: mshowalter@seti.org

Published 31 March 2011 on *Science Express*
DOI: 10.1126/science.1202241

This PDF file includes:

Materials and Methods
Figs. S1 to S5
Table S1
References

Materials, Methods and Models

1. Data Analysis

1.1 Ring Intensity Model

If a ring has spiral undulations of fixed wavelength λ and fixed amplitude Z_0 , then the vertical height of the ring surface can be defined by

$$Z(R, \theta) = Z_0 \sin(2\pi[R - R_0]/\lambda + [\theta - \theta_0]) , \quad (\text{S1})$$

using polar coordinates (R, θ) , and with (R_0, θ_0) locating any zero point of the function. The radial and longitudinal components of the surface slope are, respectively,

$$\partial Z / \partial R = Z_0 \cos(2\pi[R - R_0]/\lambda + [\theta - \theta_0]) \cdot 2\pi/\lambda \quad (\text{S2})$$

and

$$1/R \partial Z / \partial \theta = Z_0 \cos(2\pi[R - R_0]/\lambda + [\theta - \theta_0]) / R , \quad (\text{S3})$$

The radial component is larger than the longitudinal by a factor $2\pi R/\lambda \ll 1$. This justifies our neglect of the longitudinal component; we treat the local slope as simply $Z' \equiv \partial Z / \partial R$.

We describe the observed intensity of the ring as a function $I(R, \theta)$. If the ring were flat and axisymmetric, then the intensity would be

$$I_{\text{flat}}(R) = I_{\perp}(R) / \sin(B) , \quad (\text{S4})$$

where $I_{\perp}(R)$ is the intensity profile from a viewpoint perpendicular to the ring plane, and B is the ring opening angle, separating the line of sight from the equator plane. We define B to be nonnegative. The local slope of the ring changes the effective value of B . The unit surface normal vector at (R, θ) is

$$[-Z' \cos(\theta), -Z' \sin(\theta), 1] / (1 + Z'^2)^{1/2} \quad (\text{S5})$$

in rectangular coordinates $[x, y, z]$. If we define $\theta = 0$ along the ring radius vector perpendicular to the line of sight (Fig. 1A), then the unit vector pointing to the observer is

$$[0, -\cos(B), \sin(B)] \quad (\text{S6})$$

in the same coordinate frame. The complement of the angle between these vectors is the local, effective ring opening angle, B_{eff} . The inner product of Eqs. S5 and S6 determines this angle:

$$\sin(B_{\text{eff}}) = [\sin(B) + Z' \sin(\theta) \cos(B)] / (1 + Z'^2)^{1/2}. \quad (\text{S7})$$

In practice, B and Z' are both small, which leads directly to our model for intensity variations (Eq. 1):

$$I(R, \theta) = I_{\perp}(R) / \sin(B_{\text{eff}}) \approx I_{\text{flat}}(R) [1 - Z'(R, \theta) \sin(\theta) / \sin(B)]. \quad (\text{S8})$$

1.2 Image Processing

Table S1 lists the images used in this study. The Galileo images from 2000 provided our finest resolution on the Jovian ring, but required special handling to remove numerous bright spots caused by energetic particles hitting the CCD (Fig. S1). Each pixel was compared to the mean value of its four nearest neighbors, and if the difference exceeded a specified threshold, it was rejected. This process was repeated until it converged, and then the values of the rejected pixels were replaced by the local mean value.

The dark sky regions of the images are often nonzero, due to instrumental effects and to off-axis light entering the camera optics. In the Galileo images, the background light is generally rather uniform; it could be successfully modeled by a simple linear ramp function. New Horizons images were affected by a serious “ghosting” problem, however. We corrected this problem by noting that the pattern is nearly stable within the CCD, even though the rings are positioned at different locations. The rings occupy only a small portion of each image, so among the four images it became possible to map out the ghost pattern completely. This pattern was then subtracted from each of the images (Fig. S2).

We rotated each image into an orientation where the ansa line is exactly horizontal across the image. Images from the same set were adjusted and positioned to have identical geometry. This involved an iterative process using quantitative tests, such as maximizing the correlation or minimizing the root-mean-square (RMS) difference between pairs of images. We reprojected the images onto spatial grids roughly twice as fine as that of the sources; this ensured that the intrinsic spatial resolution of each image

was preserved. Within each set, the images were then co-added pixel by pixel to improve the signal-to-noise ratio. We rejected any pixels that were excessively bright in one image relative to the others, on the assumption that such pixels were probably corrupted. The combined images resulting from this processing were very clear and generally free of obvious flaws (Figs. 3A, S3).

1.3 Slope Derivation

A narrow strip of pixels centered on the ansa line of each image was resampled into a new rectangular grid in $(R, \sin(\theta))$ (Fig. S4A). To suppress noise, we employed a gaussian filter to blur the image by a few pixels prior to this step. Each column in the new image could then be described by a linear function $I = a + b \sin(\theta)$ (Eq. S8), where

$$I_{\text{flat}} = a \quad (\text{S9})$$

and

$$Z' = -b/a \sin(B) \quad (\text{S10})$$

(Fig. S4B,C; cf., 1C, 3C). We ignored the inner and outer regions of the resulting profiles $Z'(R)$, where values became highly erratic because I_{flat} was small.

1.4 Slope Modeling

For the Fourier analysis, we first trimmed away the innermost points in the slope profile, where no evidence for the ripple patterns could be seen; Figs. 1C, 3C and S4C show the ranges retained. The remaining data consists of a sequence of N radial locations R_k and slopes Z'_k . Given wavelength λ , the Fourier amplitude is defined as $(A^2 + B^2)^{1/2}$, where

$$A = 1/N \sum Z_k \cos(2\pi R_k/\lambda) \quad (\text{S11})$$

and

$$B = 1/N \sum Z_k \sin(2\pi R_k/\lambda) . \quad (\text{S12})$$

Once we identified candidate wavelengths by their peaks in the Fourier analysis, we performed non-linear, least-squares fitting to the profiles to determine the optimal

wavelength, phase and amplitude of each sinusoidal pattern. Uncertainties correspond to 1- σ confidence intervals based on χ^2 statistics.

1.5 Chirp Modeling

Because of the nonlinear dependence of nodal regression rate on the radial distance from Jupiter, the numeric coefficient in Eq. 2 actually varies by $\sim 15\%$ between radial limits of 125,000 and 129,000 km in the Jovian system; see Hedman et al. (3) for formulas and details. As a result, the radial pattern is actually a “chirp”, not a sinusoid. Successive waves can be envisioned as changing linearly:

$$\lambda = \Lambda, \Lambda[1 + \varepsilon], \Lambda[1 + 2\varepsilon], \dots \Lambda[1 + N\varepsilon] , \quad (\text{S13})$$

where Λ is the starting wavelength and $\varepsilon \ll 1$ describes the fractional change in wavelength from one cycle to the next. Successive cycles of this pattern will fall at radial locations:

$$R = 0, \Lambda, \Lambda[2 + \varepsilon], \Lambda[3 + 2\varepsilon], \dots \Lambda[N + \varepsilon (N^2 - N)/2] . \quad (\text{S14})$$

Converting the cycle number into a continuous variable x , we obtain

$$R(x) = \Lambda[x + \varepsilon x^2/2] . \quad (\text{S15})$$

However, we have chosen to model the ring patterns using a fixed wavelength λ instead:

$$R'(x) = R_0' + \lambda x . \quad (\text{S16})$$

How large are the errors that arise from this approximation? In least-squares fitting, the sinusoidal model will match the chirp as closely as is mathematically feasible, but features will necessarily shift. We estimate the magnitude of these shifts by defining $\Delta(x) \equiv R'(x) - R(x)$ and assuming that in the fitting procedure, the sinusoidal model will adjust to limit the extreme values of $|\Delta|$. Because $\Delta(x)$ is a parabola, this minimization is accomplished when

$$\Delta(0) = \Delta(N) = -\Delta(N/2) . \quad (\text{S17})$$

These equations can be readily solved for the coefficients in Eq. S16, yielding

$$\lambda = \Lambda[1 + \varepsilon N/2] ; \quad (\text{S18})$$

$$R_0' = \varepsilon \Lambda N^2 / 16 \quad (\text{S19})$$

The second equation defines $\Delta_{\max} = \Delta(0)$, the upper limit on the radial offset arising from the assumption of a fixed wavelength. If we define $\Delta R = N\lambda$ as the full radial extent of our data, and $q = \varepsilon N/2$ as the full fractional change in wavelength within this range, then

$$\Delta_{\max} = q/8 \Delta R . \quad (\text{S20})$$

Thus, although $q = 15\%$, the assumption of a fixed wavelength in our analysis introduces radial errors of only $\sim 2\%$ (80 km) in Figs. 1C and 3C. On the scale of these plots, such errors can be safely neglected.

Consistent with our intuition, a comparison of Eqs. S13 and S18 indicates that the best-fit fixed wavelength will be the value near the middle of the chirp. As a result, any determination of the elapsed time since a ripple pattern began must employ the winding rate relevant to the midpoint of the profile modeled.

2. Dynamical Models

2.1 Impact Dynamics and Tilt Amplitudes

We consider the consequences of a cometary dust grain impacting a ring particle. Working in the local frame of the ring before impact, momentum conservation can be stated

$$m_c \mathbf{v}_c = m_r' \mathbf{v}_r + m_e \mathbf{v}_e , \quad (\text{S21})$$

where m is particle mass, \mathbf{v} is velocity, and subscripts refer to the cometary impactor (c), the ring particle (r), and the impact ejecta (e). Boldface indicates a vector. For quantities that change during impact, final values are indicated by primes. Above, \mathbf{v}_e is understood to be the mass-weighted mean velocity of all ejecta after impact.

When $m_c/m_r > 10^{-7}$, a collision at tens of km/s is likely to result in catastrophic disruption (22), meaning that $m_r' \Rightarrow 0$. In this case, the initial momentum gets distributed over the total mass, and the resulting orbital tilt is

$$\begin{aligned} Z &= R v_{e\perp}/v_o \approx R (v_{c\perp}/v_o) m_c/m_r \\ &= Z_{\max} m_c/m_r . \end{aligned} \quad (\text{S22})$$

Here, v_o is the orbital velocity of the ring particle, R is its orbital radius, and subscript \perp indicates the component of \mathbf{v} perpendicular to the ring plane. For convenience, we define $Z_{\max} = R (v_{c\perp}/v_o)$, the tilt reached by a ring particle that intercepts its own mass. For the Jovian ring, $Z_{\max} \approx 130,000$ km.

Smaller impacts are non-disruptive cratering events, where yield factors are

$$Y \equiv m_e/m_c \sim 5 (v_c / [\text{km/s}])^2 \quad (\text{S23})$$

(23). In the Jovian ring, $v_c \sim 50$ km/s, implying $Y \sim 10^4$. In this limit, the initial momentum is not distributed uniformly between the ring particle and the ejecta. Energy conservation can be written

$$\begin{aligned} f m_c v_c^2 &= m_r' v_r^2 + m_e [v_e^2 + \sigma^2(v_e)] \\ &= m_r' v_r^2 + m_e g v_e^2. \end{aligned} \quad (\text{S24})$$

Here f represents the fraction of the initial energy that goes into kinetic energy, rather than heat, after impact. Because \mathbf{v}_e is the mean of a distribution, we must include $\sigma^2(v_e)$ to account for the difference between the square of the mean and the mean of the square. For convenience, we define $g \equiv 1 + \sigma^2(v_e)/v_e^2$. Combining Eqs. S23 and S24 yields a momentum ratio

$$m_r' v_r / m_c v_c \sim (Yf / g)^{1/2}. \quad (\text{S25})$$

With f and g both expected to be of order unity and $Y \sim 10^4$, we conservatively predict this ratio to be ~ 30 . The reason the value is not unity is that the ejecta systematically carry momentum away from the impact site in the opposite direction. Compared to Eq. S22,

$$Z = R v_{r\perp}/v_o = Z_{\max} m_c/m_r (Yf / g)^{1/2}. \quad (\text{S26})$$

This may appear to be gaining “something for nothing.” For an optically thick ring the ejecta would quickly deposit their opposite linear momentum elsewhere in the ring and the magnification factor would be lost. However, the Jovian ring’s optical depth $\tau \sim 10^{-5}$ (4,5) and collision time scales are measured in decades; the orbital nodes of the ejecta precess many times in the interim, preventing them from delivering any net tilt back to the ring.

Note that, because $m_c/m_r < 10^{-7}$ in Eq. S26, the largest possible tilt that can be imparted by a single, non-catastrophic collision is ~ 400 m; most deflections will be smaller. Therefore, to tilt the Jovian ring by ~ 2 km will require most particles to receive multiple impacts. Let $M(c)$ be the total integrated mass of comet particles of radius smaller than c , which pass through a ring of surface area A . The expected tilt reached by a ring particle of radius r is

$$Z(r) = Z_{\max} (Yf/g)^{1/2} \cdot M(r/K) / m_r \cdot \pi r^2 / A \quad (\text{S27})$$

This is Eq. S26 integrated over the cometary mass crossing the ring, and also scaled by the fractional cross-section of the ring particle. Here, $K \sim (10^7 \rho_c/\rho_r)^{1/3} \sim 200$ is the size ratio required for catastrophic collisions; we will show below that such impacts play a negligible role in the Jovian ring. We have assumed densities ρ_c and ρ_r are similar.

As a concrete application of Eq. S27, we define a nominal ring bounded by the orbits of Metis and Adrastea (128,000–129,000 km), yielding $A = 8 \times 10^8 \text{ km}^2$. If this ring is composed primarily of bodies with $r = 1$ cm, then $M \sim 5 \times 10^{12}$ g of cometary dust must pass through it to achieve a 2-km tilt. This corresponds to a total volume of 0.005 km^3 , exclusive of grains larger than $r/K = 50 \text{ }\mu\text{m}$.

2.2 Orbital Integrations

We carry out numerical integrations of the SL9 fragments' motion between their 1992 perijove and breakup through their July 1994 impacts. We employ a fourth-order Runge-Kutta integrator with adaptive step size. SPICE kernels obtained from the Planetary Data System (PDS) provide the positions of Jupiter, the Sun, the Galilean satellites, and Saturn, and a test particle responds accordingly. We include the J2 and J4 gravity moments of Jupiter, and allow for the effects of radiation pressure via a parameter β , which defines the ratio of the radiation pressure force to the Sun's gravity (15). By using the SPICE kernels, the problem is reduced to one of integrating individual test particles rather than integrating the entire Solar System. Other perturbations on the comet, such as those caused by outgassing and erosion, are neglected. Lorentz forces are completely negligible for particles in the size range we consider.

The SPICE kernels provide the initial position and velocity for 21 fragments of SL9 at the time of their 1992 perijove. However, the values are not sufficiently precise to integrate the fragments' motion over long periods of time. To compensate, we begin by tabulating the position of each fragment at one-day intervals from perijove to impact, using SPICE tools. We then solve for the initial state vector that minimizes the RMS residuals between the integrated and tabulated locations. Upon completion of this procedure, our integrator matches the motion of each fragment with residuals of a few hundred km. This discrepancy is small compared to the spread among the fragments' trajectories; we therefore regard our integrations as representative of SL9, even if they differ slightly from the best orbital models (11).

We then explore the perturbations needed for a particle to hit the ring instead of the planet. Typical ejection speeds of dust grains from the fragments are ~ 1 m/s (14). Neglecting radiation pressure, our integrations show that such speeds are insufficient to bypass the planet; relative speeds of ~ 30 m/s are required before the paths of ejecta can intersect the ring.

Figure 4 shows sample integrations in which solar radiation pressure has been included. Shown are the paths of dust grains through the system in 1994, after having been launched with zero initial velocity from fragment K at its 1992 perijove. In the limit of geometric optics, particle size and β are inversely related (15):

$$\beta(c) \approx 0.33 \mu\text{m}/c . \quad (\text{S28})$$

The coefficient is uncertain, depending on the albedo and density of the cometary grains, but the inverse relationship holds regardless. We adopt this relationship in the discussion to follow, while noting that uncertainty in the absolute scaling remains.

Figure 4 can be summarized by a function $\mathbf{R}(c)$, defining the ring plane intercept point for a comet particle of size c , if launched from a fragment at the time of the 1992 perijove. A more complete description of the impactors must also include their dependence on the moment t at which they are launched; this could occur at any time between the perijove and the impact ~ 742 days later. The resulting function $\mathbf{R}(c,t)$ is nearly independent of the source fragment, so we use K for all further analysis. Our integrations also reveal that small (~ 1 m/s) random velocities at the time of ejection do not change the results significantly.

Because our integrations are deterministic, for any given launch time t there exists a range of particle sizes (c_1, c_2) that will later intersect the nominal ring (Fig. S5); these are the solutions to the equations $|\mathbf{R}|(c_1, t) = 129,000$ km and $|\mathbf{R}|(c_2, t) = 128,000$ km. The mean follows a roughly linear decrease from $c_0 \approx 50$ μm at perijove to near zero just before impact. The fractional width $\Delta c/c = 0.5\text{--}0.7\%$ over this time span. At any given moment, only ejecta within a very narrow range of sizes will be launched onto paths that later intersect the ring, but *every* particle in this size range will do so. This is an idealized view of the system, surely, and neglects a variety of randomizing effects such as the slightly different trajectory of each fragment, the effects of rotation and vaporization, and the small ejection velocity of each grain. Such factors will “blur out” the narrow size distribution of ring impactors at any given moment. Nevertheless, the distribution of impactors launched at time t will still be centered on roughly the same size and will still carry a comparable fluence of mass into the ring.

2.3 Impactor Populations and Dust Fluence Estimates

We distinguish two populations of particles that serve as potential impactors into the Jovian ring. First are those grains created during the breakup event around perijove in 1992. The existence of this population (P1) is supported by early images of SL9, in which the fragments are already shrouded by a broad stream of dust (16). A second population (P2) comprises those particles that were ejected after breakup (14).

Colliding populations typically obey a power-law model, in which

$$n(c) \, dc = n_j (c/\mu\text{m})^{-p} \, dc \quad (\text{S29})$$

defines the total number of particles in the size range c to $c+dc$. The coefficient n_j has dimensions of length^{-1} , making the integral over c dimensionless. We apply the subscript $j = 1$ or 2 to distinguish models for populations P1 and P2, respectively. Exponent p is typically 2–4, which ensures that the mass of the population is dominated by the upper end of the distribution,

$$M_j(c_{\text{max}}) = 4\pi/3 \, \rho_c \, n_j (c_{\text{max}}/\mu\text{m})^{4-p} / (4-p) \, \mu\text{m}^4, \quad (\text{S30})$$

where c_{max} is the upper cutoff. For $p = 4$, both limits come into play, but the dependence is only logarithmic:

$$M_j(c_{\min}, c_{\max}) = 4\pi/3 \rho_c n_j \log(c_{\max}/c_{\min}) \mu\text{m}^4. \quad (\text{S31})$$

Population 1 was created within a short time span around perijove at $t = 0$. As the integrations illustrate, only particles in a narrow size range will intersect the ring. Total mass within this range can be expressed as a fraction of the mass in P1. It is convenient to divide P1 into the particles smaller and larger than c_o , because only the former can possibly interact with the ring. Referring exclusively to the smaller particles, the fractional mass F_1 intersecting the ring is $(\Delta c/c_o) (4-p)$ or, if $p = 4$, $(\Delta c/c_o) \log(c_{\min}/c_o)$. In either case, the coefficient on $(\Delta c_o/c_o)$ is of order unity, yielding $F_1 \sim 0.5\%$.

Population 2 was created continuously during SL9's final orbit. In this case, the information in Fig. S5 enables us to determine the fraction F_2 of particles smaller than c_o that intersect the ring. If the dust is ejected at a uniform rate, then the fraction of particles of size c intersecting the ring is simply $F_2(c) = [t_2(c) - t_1(c)]/P$, where $P \approx 742$ days is the orbital period and (t_1, t_2) are the solutions to $|\mathbf{R}|(c, t_1) = 129,000$ km and $|\mathbf{R}|(c, t_2) = 128,000$ km. We can integrate $F_2(c)$ times the size distribution to determine the total mass fraction F_2 of particles smaller than $c_o = 50 \mu\text{m}$ that intersect the ring. We find a roughly linear trend with p , with $F_2 = 0.35\%$ for $p = 2$ and $F_2 = 0.15\%$ for $p \Rightarrow 4$. The fractions F_1 and F_2 are similar, permitting us to adopt 0.2–0.5% as the fraction of SL9 dust that will intercept our nominal 1000-km wide ring.

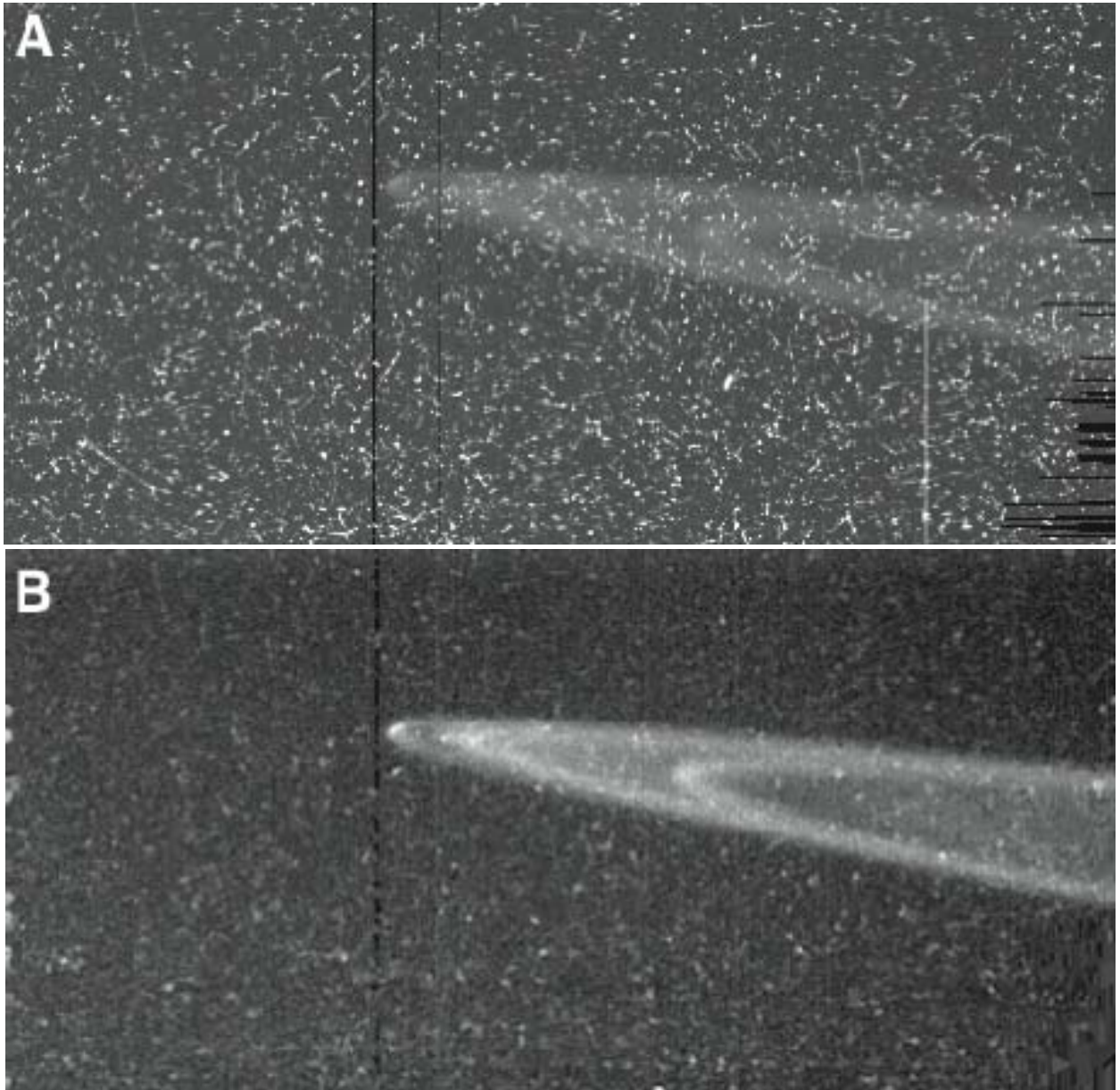


Fig. S1.

(A) Charged particles hitting the CCD created a dense overlay of corrupted pixels in Galileo image C0552599400. (B) An iterative procedure systematically masked out any pixels that were too different from their nearest neighbors. The resulting image is much cleaner. Combined analysis of this image with C0552603500, taken 39 minutes later, produced the image shown in Fig. 3A.

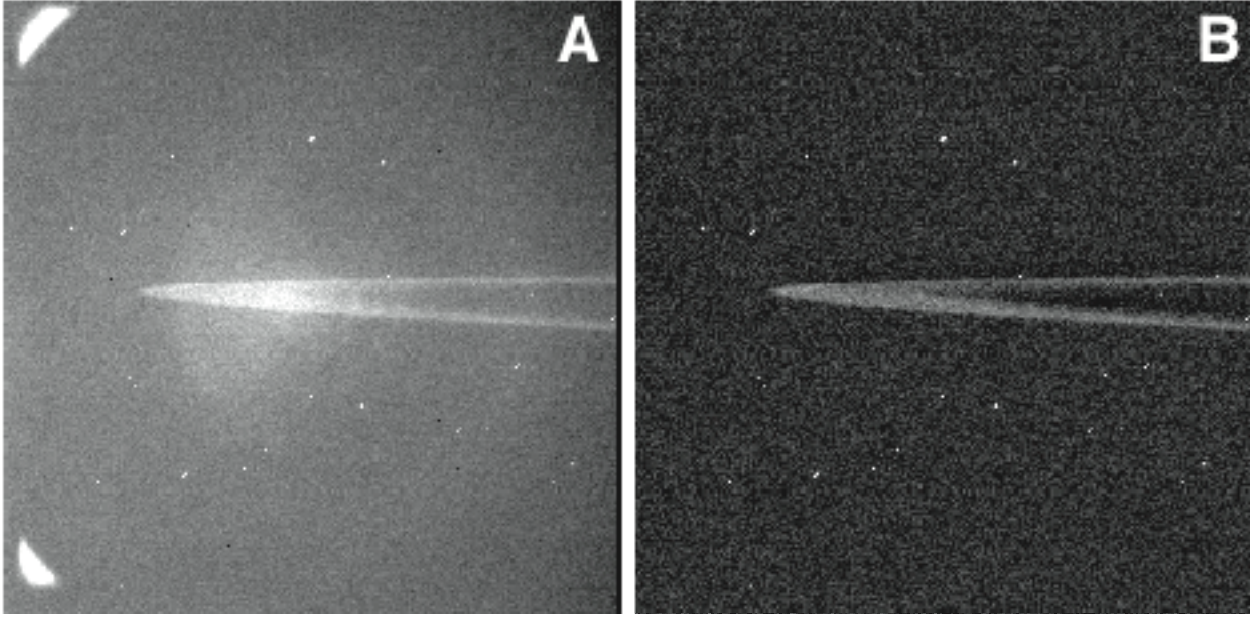


Fig. S2.

“Before” and “after” versions of New Horizons image 0035079924. (A) The image initially showed a “ghost” pattern from light scattered within the optics. However, three other images showed a similar pattern but with the ring falling at slightly different positions within the frame. This made it possible to isolate the ghost pattern and subtract it away from each image (B).

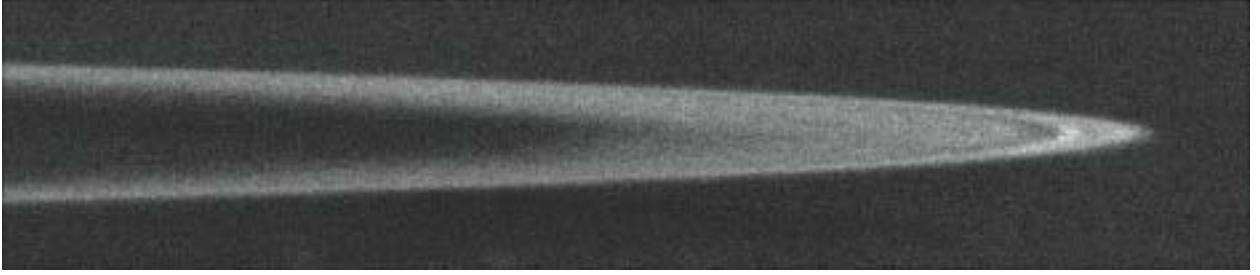


Fig. S3.

The final, rotated and co-added version of our four New Horizons images.

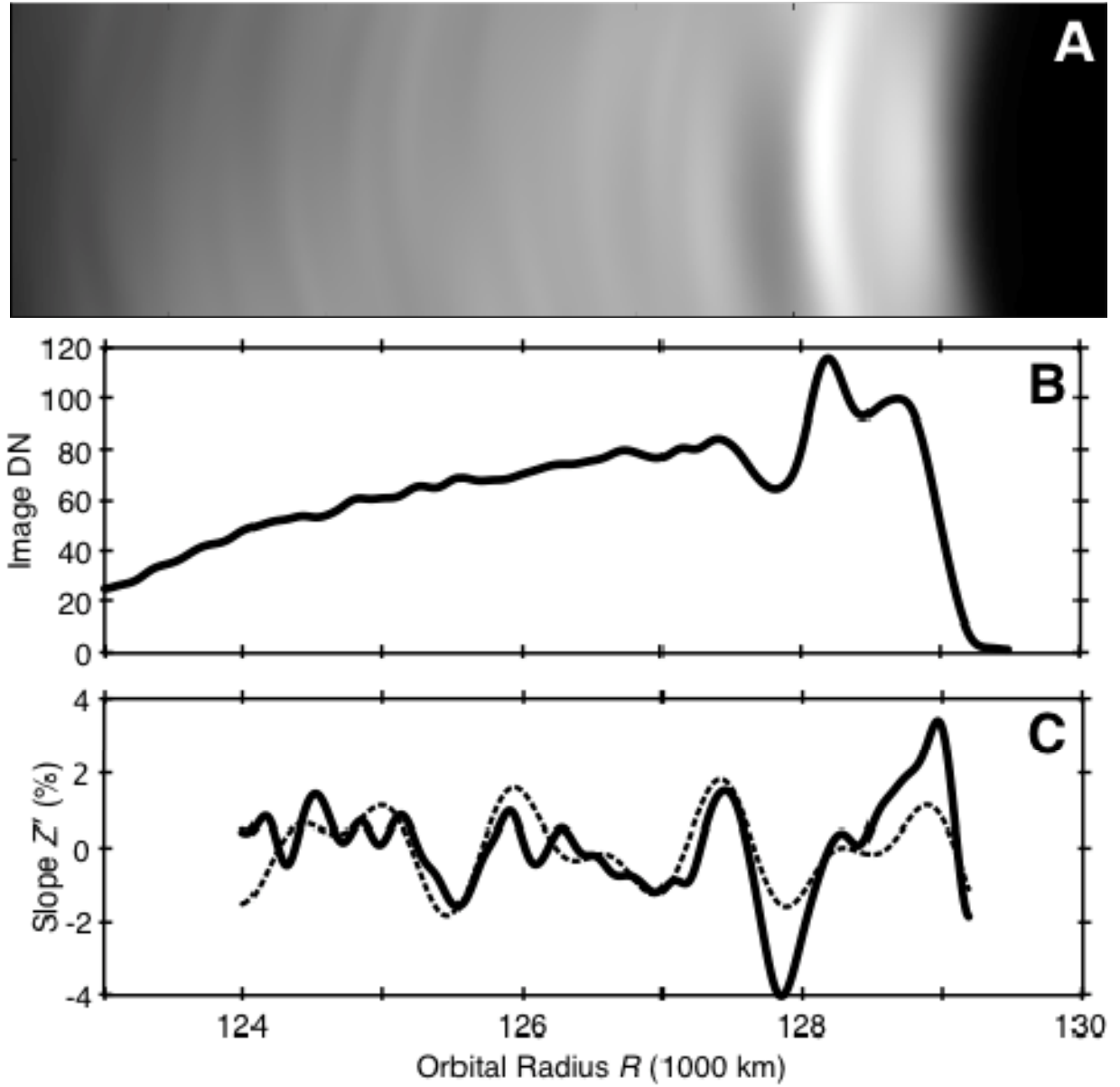


Fig. S4.

(A) The ring tip in Fig. S3 has been reprojected onto a uniform grid in $[R, \sin(\theta)]$. The columns of this image can then be modeled as described in the text to produce (B), a mean radial profile of ring intensity, I_{flat} , and (C), a model for the ring slope. The dashed line shows a best-fit model comprising two sinusoids: $\lambda_1 = 1315$ km; $Z_1 = 2.3$ km; $\lambda_2 = 775$ km; $Z_2 = 1.0$ km. The third peak in the Fourier transform, which we associate with SL9 in Fig. 2C, has a much smaller amplitude and is not included in this model.

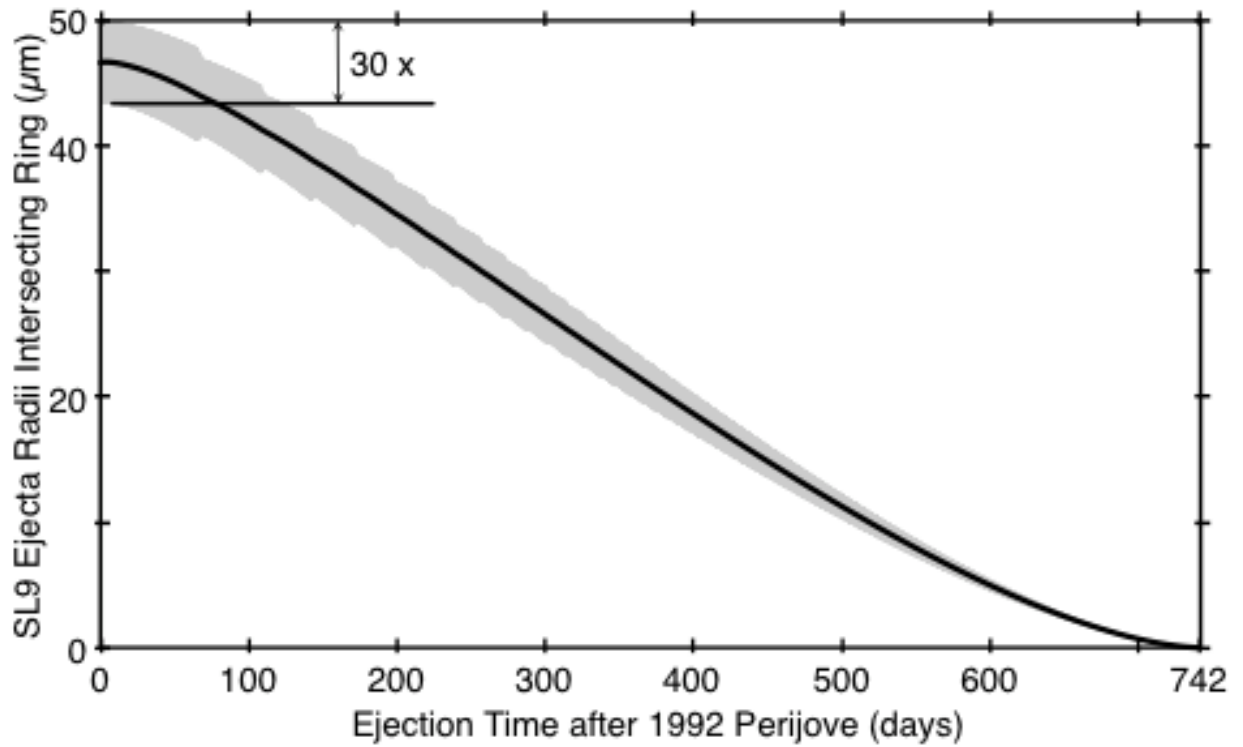


Fig. S5.

The size of a cometary dusty grain destined to impact the Jovian ring, based on the date of release at low velocity from fragment K. The gray zone represents the size range around the mean that will intersect a 1000-km wide ring. This zone has been expanded by a factor of 30 to make it more visible in the figure; typically, the vertical width is 0.5–0.7% of the mean.

Table S1.

Summary of images.

Image Set	Image ID	Observation Time	Opening Angle <i>B</i> (°)	Range to Jupiter (1000 km)	Image Resolution (km/pixel)	Phase Angle (°)
Galileo 1996						
	C0368974139	1996-11-09T04:15	0.48	2,259	22	179.2
	C0368991900	1996-11-09T07:15	0.48	2,333	23	178.3
	C0368992339	1996-11-09T07:20	0.48	2,331	23	177.6
Galileo 2000						
	C0552599400	2000-05-21T12:30	0.45	639	6.4	21
	C0552603500	2000-05-21T13:11	0.39	663	6.6	5.8
New Horizons 2007						
	0035079784	2007-03-01T18:31	0.79	3,488	17	139
	0035079854	2007-03-01T18:32	0.79	3,489	17	139
	0035079924	2007-03-01T18:33	0.79	3,490	17	139
	0035080321	2007-03-01T18:40	0.79	3,496	17	139

References and Notes

1. M. Ockert-Bell *et al.*, *Icarus* **138**, 188 (1999).
2. M. M. Hedman *et al.*, *Icarus* **188**, 89 (2007).
3. M. M. Hedman, J. A. Burns, M. W. Evans, M. S. Tiscareno, C. C. Porco, *Science*, published online 31 March 2011; 10.1126/science.1202238.
4. M. R. Showalter, J. A. Burns, J. N. Cuzzi, J. B. Pollack, *Icarus* **69**, 458 (1987).
5. S. M. Brooks, L. W. Esposito, M. R. Showalter, H. B. Throop, *Icarus* **170**, 35 (2004).
6. Materials and methods are available as supporting material on *Science Online*.
7. This formula is only valid where both $\sin(B)$ and $\sin(\theta)/\sin(B) Z'(R, \theta)$ are $\ll 1$; these constraints are satisfied throughout our analysis.
8. R. A. Jacobson, *Bull. Amer. Astron. Soc.* **33**, 1039 (2001).
9. A. Sánchez-Lavega *et al.*, *Astrophys. J.* **715**, L155 (2010).
10. L. A. Benner, W. B. McKinnon, *Icarus* **118**, 155 (1995).
11. P. W. Chodas, D. K. Yeomans, The orbital motion and impact circumstances of comet Shoemaker-Levy 9, in *The Collision of Comet Shoemaker-Levy 9 and Jupiter*, K. S. Noll, H. A. Weaver, P. D. Feldman, Eds. (Cambridge Univ. Press, 1996), pp. 1–30.
12. K. Zahnle, L. Dones, H. F. Levison, *Icarus* **136**, 202 (1998).
13. Z. Sekanina, P. W. Chodas, D. W. Yeomans, *Astrophys. J.* **289**, 607 (1994).
14. J. M. Hahn, T. W. Rettig, *Icarus* **146**, 501 (2000).
15. J. A. Burns, P. L. Lamy, S. Soter, *Icarus* **40**, 1 (1979).
16. H. A. Weaver *et al.*, *Science* **263**, 787 (1994).
17. E. Asphaug, W. Benz, *Icarus* **121**, 225 (1996).
18. Z. Sekanina, P. W. Chodas, D. K. Yeomans, *Plan. Space Sci.* **46**, 21 (1998).
19. M. Zamarashkina, Y. Medvedev, *Proc. of ACM* **500**, 457 (2002).
20. J. A. Burns *et al.*, *Jupiter's Ring-Moon System*, in *Jupiter: The Planet, Satellites and Magnetosphere*, F. Bagenal, Eds. (Cambridge Univ. Press, 2004), pp. 241–262.
21. M. R. Showalter *et al.*, *Science* **318**, 232 (2007).
22. W. Benz, E. Asphaug, *Icarus* **142**, 5 (1999).
23. E. Grün, G. E. Morfill, G. Schwehm, T. V. Johnson, *Icarus* **44**, 326 (1980).